Mapping Photothermally Induced Gene Expression in Living Cells and Tissues by Nanorod-Locked Nucleic Acid Complexes

Reza Riahi,[†] Shue Wang,[†] Min Long,[‡,§] Na Li,[⊥] Pei-Yu Chiou,[∥] Donna D. Zhang,[‡] and Pak Kin Wong[†,*]

[†]Department of Aerospace and Mechanical Engineering, University of Arizona, Tucson, Arizona 85721, United States, [‡]Department of Pharmacology and Toxicology, University of Arizona, Tucson, Arizona 85724, United States, [§]Department of Endocrinology, Xinqiao Hospital, Third Military Medical University, Chongqing 400037, People's Republic of China, [⊥]Department of Mechanical and Aerospace Engineering, University of Miami, Coral Gables, Florida 33146, Unites States, and [∥]Department of Mechanical and Aerospace Engineering, University of California, Los Angeles, California 90095, United States

ABSTRACT The photothermal effect of plasmonic nanostructures has numerous applications, such as cancer therapy, photonic gene circuit, large cargo delivery, and nanostructure-enhanced laser tweezers. The photothermal operation can also induce unwanted physical and biochemical effects, which potentially alter the cell behaviors. However, there is a lack of techniques for characterizing the dynamic cell responses near the site of photothermal operation with high spatiotemporal resolution. In this work, we show that the incorporation of locked nucleic acid probes with gold nanorods allows photothermal manipulation and real-time monitoring of gene expression near the area of irradiation in living cells and animal tissues. The multimodal gold nanorod serves as an endocytic delivery reagent to transport the probes into the cells, a fluorescence quencher and a binding competitor to detect intracellular mRNA, and a plasmonic photothermal transducer to induce cell ablation. We demonstrate the ability of the gold nanorod-locked nucleic acid complex for detecting the spatiotemporal gene expression in viable cells and tissues and inducing photothermal ablation of single cells. Using the gold nanorod-locked nucleic acid complex, we systematically characterize the dynamic cellular heat shock responses near the site of photothermal operation. The gold nanorod-locked nucleic acid complex enables mapping of intracellular gene expressions and analyzes the photothermal effects of nanostructures toward various biomedical applications.

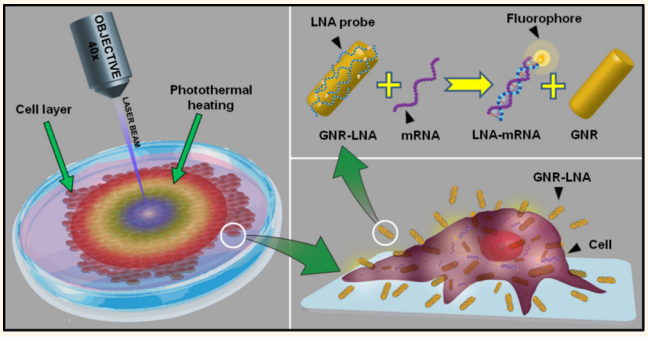

KEYWORDS: gold nanorods · locked nucleic acids · plasmonic nanostructures · photothermal effects · heat shock response · intracellular detection

The advent of plasmonic nanostructures has opened new opportunities in fundamental biology and translational medicine.[1−11] Photothermal therapy of cancer and other diseases, for instance, is based on plasmonic nanoparticle-enhanced laser absorption to treat the target cells or tissues.[4] With the leaky vasculature of tumor tissues or by specific surface functionalization, plasmonic nanoparticles can preferentially accumulate in cancer cells.[12−14] The high concentration of nanoparticles in the cancer tissue enables photothermal operation, such as localized heating and cell ablation, using near-infrared laser, which has a large penetration depth in tissue. Photothermal therapy of cancer, for instance, utilizes the plasmonic effect of gold nanorods with near-infrared laser.[4,15] Furthermore, plasmonic nanostructures coupled with small interfering RNA (siRNA) have been applied to control photonic gene circuits.[7,16] The siRNA−nanostructure technique allows optically addressable release of siRNA and provides an effective approach for precise perturbation of gene circuits without permanent genomic medications. A photothermal nanoblade has also been developed for large cargo delivery in living cells.[17] The technique utilizes a glass microcapillary pipet with a thin metal

* Address correspondence to pak@email.arizona.edu.

Received for review January 7, 2014 and accepted March 15, 2014.

Published online March 19, 2014
10.1021/nn500107g

© 2014 American Chemical Society

film sputtered onto the tip. To transfer cargo into living cells, the tip is positioned to lightly touch the membrane of a cell and a short laser pulse, which causes the formation of a nanoscale cavitation bubble due to laser–metal structure coupling at the tip to locally disrupt the contacting lipid bilayer. In addition, dielectrophoretic force can also be induced for cell manipulation by focusing a polarized laser to a gold nanoshell array or other nanostructures.[8,10] The laser excites localized surface plasmon resonance and creates high nonuniform electric field for dielectrophoretic manipulation.

In most biological and clinical applications, short laser pulses or low laser powers are applied to avoid unnecessary harmful effects to cells and tissues. With the increasing applications of plasmonic nanostructures, unwanted effects could be introduced to cells in or near the site of photothermal operation, especially in situations that require long excitation duration or high laser power.[18] In particular, localized heating could induce cellular stress responses, such as heat shock proteins (HSPs), which are molecular components in the cellular defense mechanism against environmental insults. For photothermal therapy, the upregulation of heat shock protein may enhance tumor cell imparting resistance to chemotherapy and potentially increases tumor recurrence induced by heat stress.[19−22] Furthermore, excessive heating to the neighboring regions could damage the healthy tissues. Despite its importance, little is known about the spatiotemporal gene expression distribution for viable cells and tissues near the region of photothermal operation.

In this study, we incorporate locked nucleic acid (LNA) probes with gold nanorods (GNRs) for monitoring the spatiotemporal gene expression near the site of photothermal operation. LNA probes for detecting intracellular mRNAs are designed and characterized in viable human cells and mice tissues. The effects of laser power and duration on the spatiotemporal temperature distribution are measured and correlated with the gene expression profiles measured by the GNR–LNA complexes. Computational analysis is also performed to elucidate the heat transfer characteristics and optimize the irradiation conditions for single-cell photothermal ablation. Furthermore, the dynamic cellular heat shock responses under different conditions are characterized systematically near the site of photothermal operation.

RESULTS AND DISCUSSION

Figure 1a illustrates the design of the GNR–LNA complex for mapping photothermally induced gene expression in living cells and tissues. Detection of intracellular mRNA in individual cells is achieved by taking advantage of the gold nanoparticles' intrinsic quenching property[23−27] and the gold nanoparticle–nucleic acid binding affinity.[28] In this approach, 5′ fluorescently labeled LNA probes with alternating LNA/DNA monomers are attached to GNRs, spontaneously forming GNR–LNA complexes. Alternating LNA/DNA monomers were previously shown to improve the probe stability for intracellular detection and adjust the binding affinity.[29−32] In the absence of a target mRNA, the fluorophore conjugated to the LNA probe is quenched due to proximity with the GNR. With the specific target, the LNA probe is displaced from the GNR thermodynamically and hybridizes to the mRNA, allowing the fluorophore to fluoresce.

We characterized the GNR–LNA complexes for intracellular detection in human breast adenocarcinoma cells and mice tissues. Figure 1b shows the intensity of LNA probes targeting β-actin and heat shock protein 70 (*HSP70*) in the alveolar structures of mice lung tissues. High intensities were observed for the probes. In contrast, the random probe had a low intensity throughout the experiment. Similar results were observed in MCF7 cells and mice liver tissues (Supporting Information Figure S1). Furthermore, the GNR effectively quenched the fluorophore and displayed a quenching efficiency 2.4 times higher than an organic quencher conjugated to a complementary LNA/DNA sequence (Figure S2a,b). The specificity of the assay was tested by the random probe control (Figure S2c). Without a target, both probes exhibited a low background level comparable to the buffer solution. The β-actin target significantly increased the intensity of the β-actin probe but not the random probe, demonstrating the specificity of the assay. To examine the effect of laser irradiation, laser was irradiated to the GNR–LNA solution and did not show any observable effect (Figure S2d). These results collectively support the effectiveness of the GNR–LNA complex for gene expression analysis.

With GNRs, individual cells in tissues and monolayer cultures could also be selectively ablated by focusing the laser to the cell (Figure 1c and movie S1). Control experiments without GNRs were also performed (movie S2). We utilized UV–vis–NIR spectrophotometry to measure the absorption spectrum of the GNR for optimizing the photothermal effect (Figure S3a). The length and width of the GNR were 67 and 10 nm, and there were two peaks at 900 and 570 nm corresponding to the longitudinal and transverse surface plasmon resonance modes.[33] Dark-field images illustrated that the uptake of GNRs was uniform among the cells (Figure 2a,b and Figure S3b). To determine the amount of GNRs in the cell, we performed inductively coupled plasma mass spectrometry measurement after 12 h of incubation (Figure S3c). The amount of intracellular GNR could be controlled by adjusting the concentration of GNR during incubation. With an appropriate concentration (*e.g.*, 4000 GNRs/cell), the GNRs displayed minimal cell toxicity, as indicated by cell morphology and viability, and provided an optimum photothermal effect

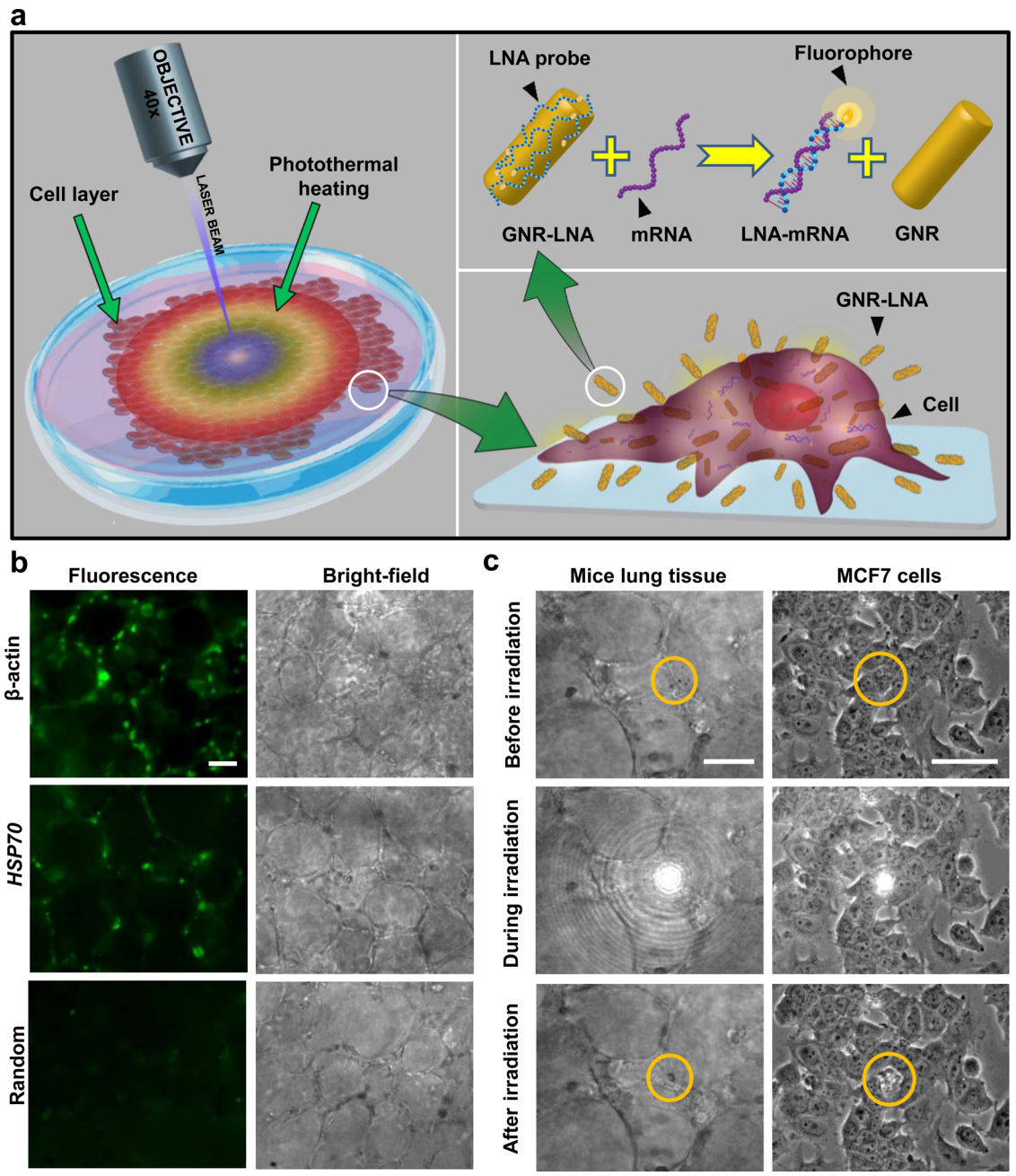

Figure 1. Multimodal GNR–LNA complexes for intracellular gene expression mapping and photothermal operation. (a) Schematic of the photothermal experiment. To induce photothermal effects, the laser was focused to a cell of interest. The laser energy is coupled by the plasmonic GNRs in the cells. The GNR also delivers the LNA probes into the cells and quenches the fluorophore conjugated to the probe. With a target mRNA, the probe displaces from the GNR and hybridizes to the target, allowing intracellular gene expression analysis in living cells and tissues. (b) Intracellular gene expression of β-actin and *HSP70* mRNAs in mice lung tissues. A random sequence is designed as the negative control. The fluorescence intensity in the cytoplasm of each cell can be extracted from the images to map the spatiotemporal gene expression dynamics. Scale bar, 50 μm. (c) Photothermal ablation experiment performed by focusing the laser to a target cell of interest in mice lung tissues (left) and monolayer cultures (right). Cycles indicate the target cell in the ablation experiments. Scale bars, 50 μm. Data are representative images from three independent experiments.

(Figure S3d,e).[34−37] This concentration was thus used throughout this study.

The photothermal temperature elevation at this GNR concentration was then characterized using miniaturized thermocouples (10 μm diameter) and an infrared camera. With continuous irradiation to a target cell (150 mW; 15 μm beam size) for 1 min, a temperature gradient was established and cells nearby experienced different temperatures depending on their positions (Figure 2c,d). The temperature rise at the irradiation site could be controlled from 2 to 15 °C by adjusting the laser power (Figure 2e). Without GNRs, the temperature was only modulated slightly (<2 °C), and the cells did not show any observable effect (Figure S3f,g).

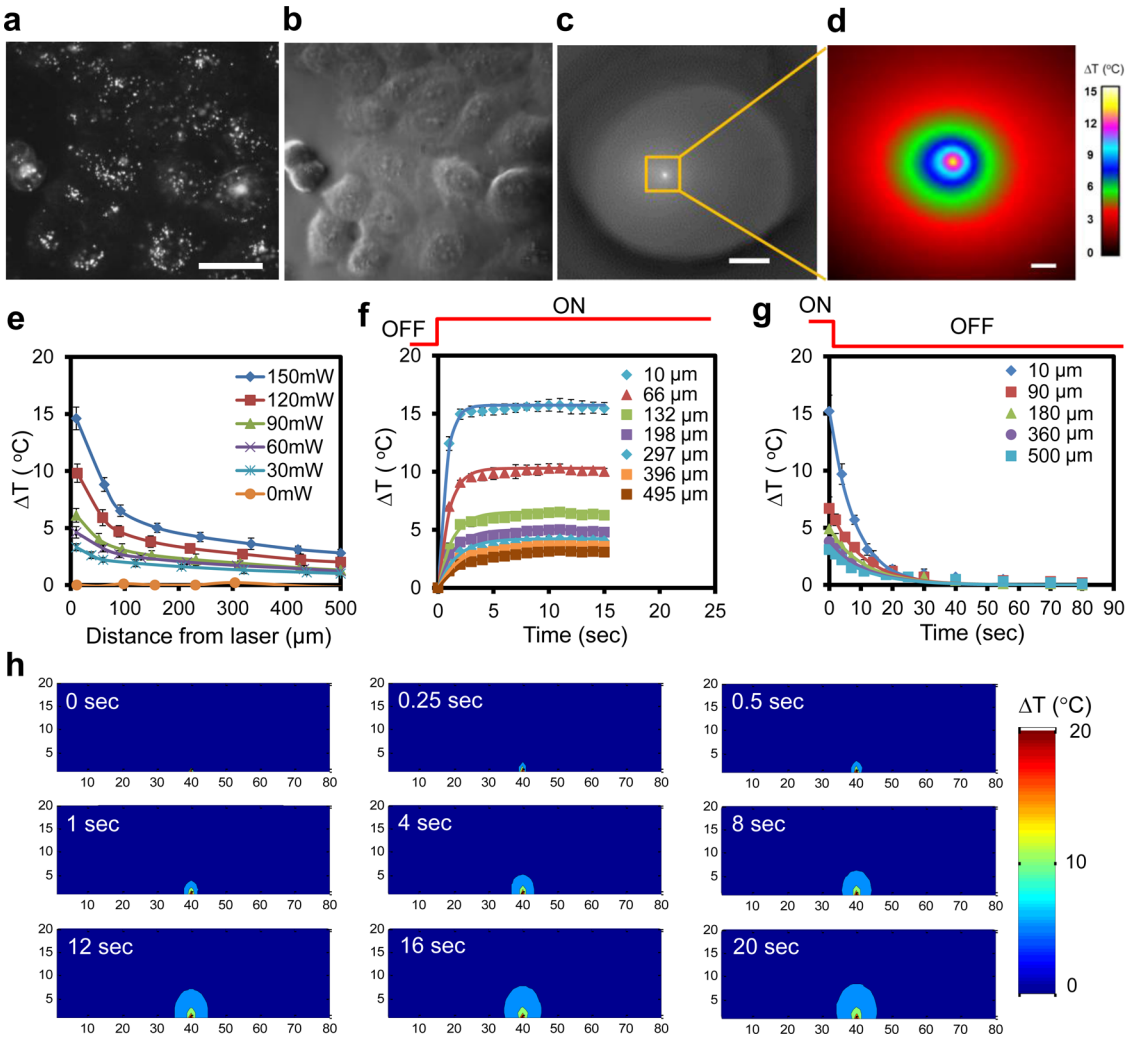

Figure 2. Characteristics of GNR for photothermal operation. (a,b) Dark-field and bright-field images for characterizing cellular uptake of GNRs. The cells were incubated with 2×10^{11} GNR/mL for 12 h. Scale bar, 25 μm. (c) Infrared thermometry for measuring the temperature profile in a glass bottom tissue culture dish. A single cell is irradiated by the laser to induce localized photothermal heating. Scale bar, 1 mm. (d) Temperature distribution near the laser. Scale bar, 150 μm. Color bar indicates the temperature elevation with respect to the reference temperature (37 °C). (e) Temperature distributions near the laser with different values of laser power after 1 min irradiation. Laser was focused at the origin. (f) Heating experiments measured by miniaturized thermocouples with laser irradiation at 150 mW. Data were fitted with exponential functions to extract the heating time constants. (g) Thermal cooling experiments monitored by miniaturized thermocouples. Data were fitted with exponential functions to extract the cooling time constants. (h) Computational simulation illustrating the evolution of the spatial temperature profiles with continuous laser irradiation. The simulation domain consists of 1600 elements, and each element represents 100 μm by 100 μm. The size of the domain is 2 mm by 8 mm. Color bar indicates the amplitude of temperature elevation.

To determine the heat transfer characteristics, we performed thermal cooling and heating experiments. The heating time constants were between 1 and 4 s depending on the distance from the laser (Figure 2f). A longer constant in the range of 15−25 s was observed for cooling (Figure 2g). To elucidate the heat transfer process, a numerical simulation was also performed (Figure 2h and Figures S4−S7). Effects of laser duration on the temperature profile are described in supplementary section B and movies S3−S6. The results were in good agreement with the experiments and revealed that the thermal time constants are related to the convective heat transfer at the boundary and the heat accumulation of the bulk solution.

To examine the spatial cellular heat shock responses, the intensity distributions of the *HSP70* probes were measured in human cells and mice lung tissues (Figure S8 and Figure 3). The laser beam size was focused to smaller than a cell (~15 μm) with an optical intensity of 0.85 mW/μm^2. The *HSP70* expressions were examined before and after laser irradiation in lung tissues (Figure 3a,b). The spatial gene expression profiles were dependent upon the irradiation duration. For 5 min irradiation, the gene expression in neighboring cells near the irradiation area was upregulated and displayed a gradient in response (Figure 3c. With longer irradiation (*e.g.*, 15 or 30 min), the cell response was upregulated in 100−300 μm away from the laser and

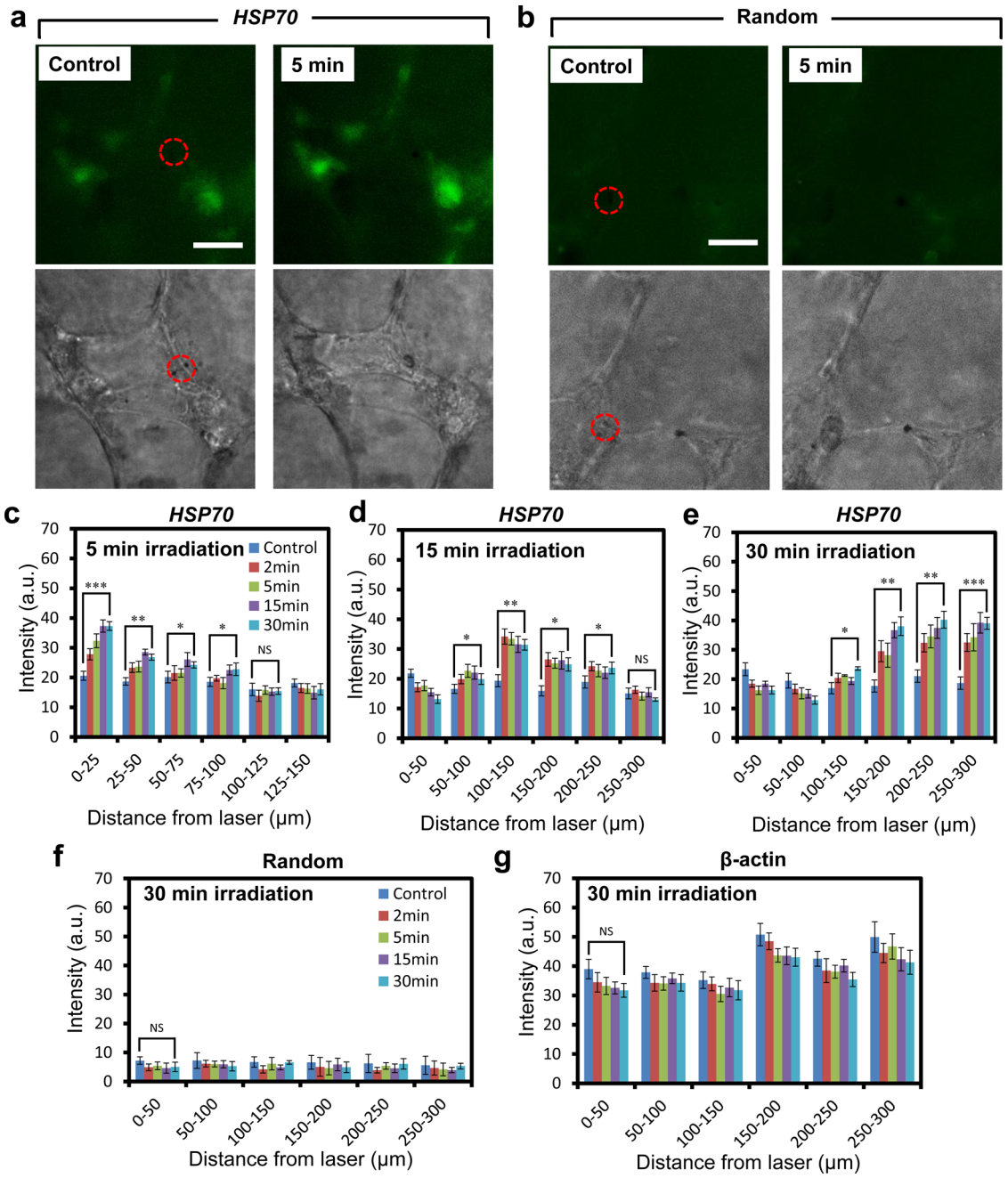

Figure 3. Mapping of *HSP70* gene expression distributions induced by laser irradiation of single cells. (a,b) Fluorescence and bright-field images before and after 5 min of laser irradiation. The LNA probes target *HSP70* mRNA and a random sequence. Red circles indicate the locations of laser irradiation in lung tissues. Scale bar, 25 μm. (c–e) Intercellular gene expression distribution in different locations. Laser was focused at the origin. Intensity was measured before and at 2, 5, 15, and 30 min after laser irradiation. The experiment was repeated with 5, 15, and 30 min of laser irradiation. A single cell was irradiated in each experiment. (f,g) Laser irradiation experiments were performed using the random and β-actin probes with 30 min irradiation. All other conditions were the same as the *HSP70* experiments. Statistical analysis, $n = 3$ (NS, not significant; *$P < 0.05$; **$P < 0.01$; ***$P < 0.001$).

was downregulated in the vicinity of the laser (Figure 3d,e). To confirm that the observed gene expression response is not a result of thermal dissociation of the GNR–LNA complexes, the random and β-actin probes were used as control, showing uniform intensities throughout the experiment (Figure 3f,g). The intensities were primarily compared between different time points at the same location due to the random distribution of the initial intensity. This observation confirmed that the temperature elevation induced at different distance from the heat source did not induce nonspecific release of the probes from the GNRs inside the cells. The general trend of the spatiotemporal gene expression responses was similar in MCF7 cell cultures, despite the differences in architectures, heat transfer characteristics, and cell types (Figure S8).

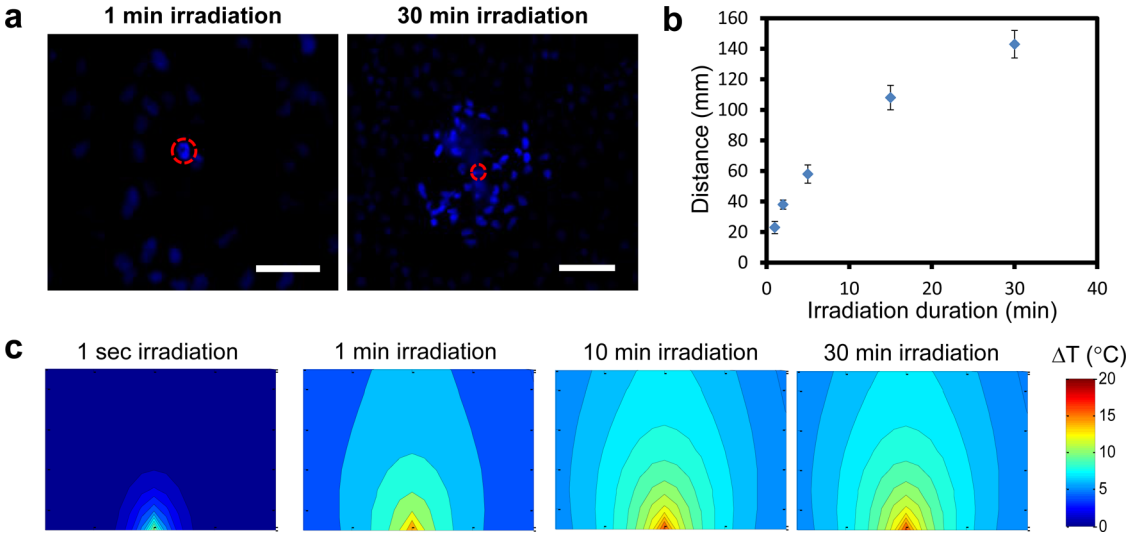

Figure 4. (a) Cell apoptosis measurement using Hoechst 33342. The distributions of apoptotic cells after 1 and 30 min of laser irradiation. Scale bars, 50 μm (left) and 100 μm (right). (b) Region of cell death as a function of the duration of laser irradiation. (c) Computational simulation showing the temperature distribution for different durations of laser irradiation. The domain of the simulation was 2 mm by 8 mm. Only the temperature near the laser (2 mm by 2 mm) is shown to illustrate the local temperature distribution. Color bar indicates the amplitude of temperature elevation.

To investigate the reduction of *HSP70* expression near the laser at long irradiation, the cells were evaluated with a fluorescent apoptosis assay. Figure 4a shows the distribution of apoptotic cells relative to the location of laser irradiation. With a short duration (*e.g.*, 1 min or less), cell ablation was achieved at the single-cell level (~25 μm). Increasing the duration expanded the region of apoptotic cells (Figure 4b), which correlated to the area of *HSP70* reduction. For instance, 30 min of irradiation induced cell apoptosis in a region ~140 μm from the laser. The *HSP70* reduction and cell apoptosis near the site of photothermal operation were determined by the coupled effects of spatial temperature profile and the duration that cells experienced the elevated temperature. With continuous irradiation, heat accumulation was observed in the bulk solution, which extended the high-temperature region (Figure 4c). The elevated temperature reduced *HSP70* expression and induced cell apoptosis. Collectively, these results revealed the effects of irradiation duration on the cellular heat shock stress response and determined the length scale of photothermal damage on neighboring cells.

We further analyzed the dynamic response of *HSP70* mRNA induced photothermally (Figure 5 and Figures S9 and S10). With a short duration of irradiation (*e.g.*, 1−2 min), the cells near the laser exhibited only a small elevation of *HSP70* mRNA expression. With longer irradiation durations, the *HSP70* expression for most cells within 100−400 μm increased asymptotically toward temperature-dependent steady-state values. Figure 5a−c shows the heat shock response between 40 and 44 °C. We excluded the data for the cells experiencing high temperature (>44 °C) due to the loss of *HSP70* expression. The data followed the first-order kinetics, allowing the time constants and amplitudes to be extracted (Figure 5d). The time constant increased linearly with respect to the irradiation time, suggesting the cell actively responded to continuous irradiation (Figure 5e). Remarkably, the time constant was insensitive to temperature between 40 to 44 °C. In contrast, the amplitude of *HSP70* expression increased with both irradiation time and temperature in a nonlinear manner (Figure 5f). The cells near the laser responded to both amplitude and duration of laser irradiation dynamically, highlighting the complex cellular heat shock response and the importance of monitoring cellular responses during photothermal manipulation.

In this study, we demonstrate the multimodal GNR approach for photothermal operation and monitoring the spatiotemporal gene expression in living cells and tissues. The technique allows us to study the dynamic cellular response induced photothermally. In particular, heat shock triggers multiple signaling pathways and complex regulation of gene expression in cells and tissues.[38,39] Our *HSP70* mRNA and cell viability data illustrate the complex spatiotemporal dynamics in which the combined effects of irradiation duration and associated temperature elevation are critical during photothermal operation and should be considered for utilizing plasmonic nanostructures. This is particularly important in cases that require high laser power or long duration, such as cancer photothermal therapy, tissue ablation, physical manipulation of cells, and gene manipulation. Previous characterization of the photothermal response primarily relied on immunochemistry and RNA *in situ* hybridization in fixed cells and tissues. These techniques have limited abilities to measure the spatiotemporal gene expression profiles and to reveal the characteristics of the dynamic heat

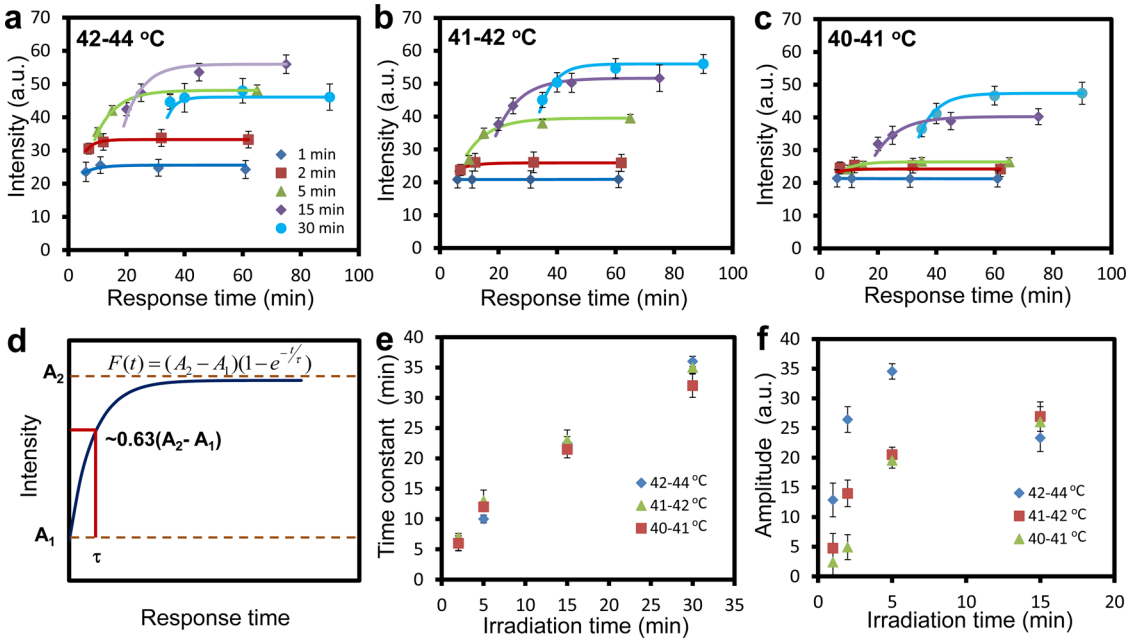

Figure 5. Dynamics of *HSP70* expression and regulation. (a–c) Dynamic intensity profiles of *HSP70* probes under different temperatures and irradiation durations. Lines are curve fitting using the equation defined in d. (d) Kinetic equation for estimating the time constant, τ, and amplitude, A_2-A_1. (e,f) Time constants and amplitudes of *HSP70* expression extracted from data in a–c. Each data point is an average of at least 50 cells from three independent experiments. The data are expressed as mean ± SEM.

shock response. With its simplicity and effectiveness for mapping intracellular gene expression, the multimodal GNR–LNA is anticipated to serve as a platform technology for characterizing the cell behaviors during photothermal manipulations and optimizing the performance of plasmonic nanostructures toward a wide spectrum of biomedical applications in the future.

CONCLUSIONS

In summary, we demonstrate a GNR–LNA complex for monitoring intracellular gene expression in living cells and tissues. The gold nanorod quenches the fluorophore with high efficiency and allows intracellular delivery to living cells and tissues without the requirement of transfection reagents or microinjection. Furthermore, the complex enables us to monitor the dynamic gene expression of cells near the site of photothermal operation. The GNR–LNA represents a highly effective approach for intracellular gene expression analysis and has the potential for characterizing the photothermal effects of nanostructures in a wide spectrum of biomedical applications.

MATERIALS AND METHODS

Cell Culture. Human breast adenocarcinoma cells (MCF7) were obtained from American Type Culture Collection (ATCC HTB22). Cells were cultured in Dulbecco's modified Eagle medium (Invitrogen) supplemented with 10% deactivated fetal bovine serum (Gemini BioProducts), 2 mM HEPES buffer (Sigma Aldrich), and 0.1% gentamycin (GIBCO).

Mice Tissues. Female C57BL/6 mice were fed on laboratory food and tap water *ad libitum* in a regular 12 h dark/light cycle. Preparation of precision-cut lung slices (PCLS) was performed as previously described.[40] Six weeks old mice were anesthetized through IP injection of 240 mg/kg avertin (2-2-2 tribromoethanol, Sigma Aldrich). The skin was dissected from the abdomen to the neck, and the pleural cavity and trachea were exposed. The trachea was cannulated, and the animals were exsanguinated by cutting aortaventralis. Lungs were filled *in situ* with 38 °C 0.75% agarose (Research Products International Corp.) in minimal essential medium (MEM) and covered with ice for 10 min. Lungs were removed from the thoracic cavity into a plate filled with PBS and cooled on ice for an additional 10 min. Ten millimeter diameter tissue cores were prepared using a sharpened stainless steel tube. Lung tissue cores were cut with a Brendel/Vitron Tissue Slicer (VITRON. Inc.) into 500–600 μm thin slices. Lung slices were incubated in MEM with 0.5% gentamycin at 37 °C, 5% CO_2, and 100% air humidity under cell culture conditions. Incubation medium was changed every 30 min for 2 h after slicing, and followed by a change every hour for the next 2 h, in order to remove agarose residues and cell debris from the tissue slices. To prepare precision-cut liver slices, the livers were placed into ice cold PBS for 10 min. Ten millimeter diameter tissue cores were prepared using a sharpened stainless steel tube. Liver tissue cores were then cut into thin slices (500–600 μm). Liver slices were incubated in MEM with 0.5% gentamycin at 37 °C, 5% CO_2, and 100% air humidity for 90 min. The University of Arizona Institutional Animal Care and Use Committee approved all animal work and protocols.

Photothermal Ablation. Cell monolayers cultured on glass bottom culture dishes were incubated with different concentrations of GNRs, including 10^{10} GNR/mL, 2×10^{11} GNR/mL, and 5×10^{11} GNR/mL, for 12 h. Quantification of GNR internalized is described in supplementary section A. In the photothermal experiment, a 1064 nm fiber laser with stable high-quality TEM^{00} beam was utilized for laser irradiation. The laser module was attached to the microscope (Nikon, TE2000-U) through an epi-fluorescence port. To optimize the conditions, individual

cells were targeted at laser powers between 0 to 150 mW with a 40× objective, which focused the laser to 15 μm. For tissue studies, mice tissues were first incubated with 2×10^{11} GNR/mL for 12 h and then placed on glass bottom dish for single-cell ablation with irradiation intensity of 0.85 mW/μm^2.

Gene Expression Mapping. We designed probes for β-actin mRNA as a positive control and *HSP70* mRNA to study the cellular responses induced photothermally. A random probe sequence was also designed as the negative control to evaluate the selectivity of the assay. The specificity of the probe sequences has previously been tested and verified.[31] The cell monolayer and mice tissues were cultured in serum-free medium for 30 min before the GNR–LNA complexes were introduced with a concentration of 2×10^{11} GNR/mL for 12 h. To induce the photothermal effect, laser with 0.85 mW/μm^2 power density was irradiated to individual cells for durations of 1, 2, 5, 15, and 30 min. To determine the spatial gene expression profile near the laser, the fluorescence intensity of intracellular gene expression was measured at different locations. To measure the dynamic changes of gene expression, the intensity profiles of cells were monitored at different time points.

Imaging. Gene expression mapping with GNR–LNA complexes of living cells and tissues, and immunostaining experiments were performed using the inverted fluorescence microscope. Bright-field and fluorescence images were captured using an HQ2 CCD camera (Photometric, Tucson, AZ). For fluorescence microscopy, all images were taken with the same exposure time and conditions for comparing the intensity. To characterize GNR internalization, dark-field images were recorded by observing scattered light using a Nikon dark-field condenser (dry, 0.95–0.80 NA) coupled with the microscope. Data collection and imaging analysis were performed using the NIH ImageJ software.

Conflict of Interest: The authors declare no competing financial interest.

Acknowledgment. The authors thank Marek Romanowski, Gabe Orsinger, and Mary Kay Amistadi for assistance in UV–vis–NIR spectrophotometry and ICP-MS. This work was supported by National Institutes of Health Director's New Innovator Award (1DP2OD007161-01) and the National Cancer Institute (5R01CA154377-02).

Supporting Information Available: Additional experimental methods, numerical analysis, and supplementary figures are available. This material is available free of charge *via* the Internet at http://pubs.acs.org.

REFERENCES AND NOTES

1. Jung, H. S.; Kong, W. H.; Sung, D. K.; Lee, M. Y.; Beack, S. E.; Keum, D. H.; Kim, K. S.; Yun, S. H.; Hahn, S. K. Nanographene Oxide–Hyaluronic Acid Conjugate for Photothermal Ablation Therapy of Skin Cancer. *ACS Nano* **2014**, *8*, 260–268.
2. Kim, J. W.; Galanzha, E. I.; Shashkov, E. V.; Moon, H. M.; Zharov, V. P. Golden Carbon Nanotubes as Multimodal Photoacoustic and Photothermal High-Contrast Molecular Agents. *Nat. Nanotechnol.* **2009**, *4*, 688–694.
3. Jang, B.; Park, J. Y.; Tung, C. H.; Kim, I. H.; Choi, Y. Gold Nanorod–Photosensitizer Complex for Near-Infrared Fluorescence Imaging and Photodynamic/Photothermal Therapy *in Vivo*. *ACS Nano* **2011**, *5*, 1086–1094.
4. Huang, X.; El-Sayed, I. H.; Qian, W.; El-Sayed, M. A. Cancer Cell Imaging and Photothermal Therapy in the Near-Infrared Region by Using Gold Nanorods. *J. Am. Chem. Soc.* **2006**, *128*, 2115–2120.
5. Wu, T. H.; Teslaa, T.; Kalim, S.; French, C. T.; Moghadam, S.; Wall, R.; Miller, J. F.; Witte, O. N.; Teitell, M. A.; Chiou, P. Y. Photothermal Nanoblade for Large Cargo Delivery into Mammalian Cells. *Anal. Chem.* **2011**, *83*, 1321–1327.
6. Chen, C. C.; Lin, Y. P.; Wang, C. W.; Tzeng, H. C.; Wu, C. H.; Chen, Y. C.; Chen, C. P.; Chen, L. C.; Wu, Y. C. DNA–Gold Nanorod Conjugates for Remote Control of Localized Gene Expression by Near Infrared Irradiation. *J. Am. Chem. Soc.* **2006**, *128*, 3709–3715.
7. Lee, S. E.; Sasaki, D. Y.; Park, Y.; Xu, R.; Brennan, J. S.; Bissell, M. J.; Lee, L. P. Photonic Gene Circuits by Optically Addressable siRNA–Au Nanoantennas. *ACS Nano* **2012**, *6*, 7770–7780.
8. Miao, X. Y.; Wilson, B. K.; Pun, S. H.; Lin, L. Y. Optical Manipulation of Micron/Submicron Sized Particles and Biomolecules through Plasmonics. *Opt. Express* **2008**, *16*, 13517–13525.
9. Suzuki, M.; Toyoda, N.; Shimojou, M.; Takagi, S. Infrared Laser-Induced Gene Expression in Targeted Single Cells of Caenorhabditis Elegans. *Dev. Growth Differ.* **2013**, *55*, 454–461.
10. Wilson, B. K.; Mentele, T.; Bachar, S.; Knouf, E.; Bendoraite, A.; Tewari, M.; Pun, S. H.; Lin, L. Y. Nanostructure-Enhanced Laser Tweezers for EfficientTtrapping and Alignment of Particles. *Opt. Express* **2010**, *18*, 16005–16013.
11. Chen, X.; Chen, Y.; Yan, M.; Qiu, M. Nanosecond Photothermal Effects in Plasmonic Nanostructures. *ACS Nano* **2012**, *6*, 2550–2557.
12. Farokhzad, O. C.; Langer, R. Impact of Nanotechnology on Drug Delivery. *ACS Nano* **2009**, *3*, 16–20.
13. Ferrari, M. Cancer Nanotechnology: Opportunities and Challenges. *Nat. Rev. Cancer* **2005**, *5*, 161–171.
14. Chow, E. K.; Ho, D. Cancer Nanomedicine: from Drug Delivery to Imaging. *Sci. Transl. Med.* **2013**, *5*, 216rv4.
15. Fang, J.; Chen, Y. C. Nanomaterials for Photohyperthermia: A Review. *Curr. Pharm. Des.* **2013**, *19*, 6622–6634.
16. Anikeeva, P.; Deisseroth, K. Photothermal Genetic Engineering. *ACS Nano* **2012**, *6*, 7548–7552.
17. Wu, T. H.; Teslaa, T.; Teitell, M. A.; Chiou, P. Y. Photothermal Nanoblade for Patterned Cell Membrane Cutting. *Opt. Express* **2010**, *18*, 23153–23160.
18. Coppens, Z. J.; Li, W.; Walker, D. G.; Valentine, J. G. Probing and Controlling Photothermal Heat Generation in Plasmonic Nanostructures. *Nano Lett.* **2013**, *13*, 1023–1028.
19. Madersbacher, S.; Grobl, M.; Kramer, G.; Dirnhofer, S.; Steiner, G. E.; Marberger, M. Regulation of Heat Shock Protein 27 Expression of Prostatic Cells in Response to Heat Treatment. *Prostate* **1998**, *37*, 174–181.
20. Gibbons, N. B.; Watson, R. W.; Coffey, R. N.; Brady, H. P.; Fitzpatrick, J. M. Heat-Shock Proteins Inhibit Induction of Prostate Cancer Cell Apoptosis. *Prostate* **2000**, *45*, 58–65.
21. Soti, C.; Nagy, E.; Giricz, Z.; Vigh, L.; Csermely, P.; Ferdinandy, P. Heat Shock Proteins as Emerging Therapeutic Targets. *Br. J. Pharmacol.* **2005**, *146*, 769–780.
22. Ciocca, D. R.; Clark, G. M.; Tandon, A. K.; Fuqua, S. A. W.; Welch, W. J.; Mcguire, W. L. Heat-Shock Protein-Hsp70 in Patients with Axillary Lymph Node-Negative Breast-Cancer—Prognostic Implications. *J. Natl. Cancer Inst.* **1993**, *85*, 570–574.
23. Fan, C. H.; Wang, S.; Hong, J. W.; Bazan, G. C.; Plaxco, K. W.; Heeger, A. J. Beyond Superquenching: Hyper-Efficient Energy Transfer from Conjugated Polymers to Gold Nanoparticles. *Proc. Natl. Acad. Sci. U.S.A.* **2003**, *100*, 6297–6301.
24. Dubertret, B.; Calame, M.; Libchaber, A. J. Single-Mismatch Detection Using Gold-Quenched Fluorescent Oligonucleotides. *Nat. Biotechnol.* **2001**, *19*, 365–370.
25. Seferos, D. S.; Giljohann, D. A.; Hill, H. D.; Prigodich, A. E.; Mirkin, C. A. Nano-Flares: Probes for Transfection and mRNA Detection in Living Cells. *J. Am. Chem. Soc.* **2007**, *129*, 15477–15479.
26. Cho, H.; Yeh, E. C.; Sinha, R.; Laurence, T. A.; Bearinger, J. P.; Lee, L. P. Single-Step Nanoplasmonic VEGF165 Aptasensor for Early Cancer Diagnosis. *ACS Nano* **2012**, *6*, 7607–7614.
27. Prigodich, A. E.; Randeria, P. S.; Briley, W. E.; Kim, N. J.; Daniel, W. L.; Giljohann, D. A.; Mirkin, C. A. Multiplexed Nanoflares: mRNA Detection in Live Cells. *Anal. Chem.* **2012**, *84*, 2062–2066.
28. Maxwell, D. J.; Taylor, J. R.; Nie, S. M. Self-Assembled Nanoparticle Probes for Recognition and Detection of Biomolecules. *J. Am. Chem. Soc.* **2002**, *124*, 9606–9612.
29. Campbell, M. A.; Wengel, J. Locked *vs*. Unlocked Nucleic Acids (LNA *vs*. UNA): Contrasting Structures Work towards Common Therapeutic Goals. *Chem. Soc. Rev.* **2011**, *40*, 5680–5689.
30. Wu, Y. R.; Yang, C. J.; Moroz, L. L.; Tan, W. H. Nucleic Acid Beacons for Long-Term Real-Time Intracellular Monitoring. *Anal. Chem.* **2008**, *80*, 3025–3028.

31. Riahi, R.; Dean, Z.; Wu, T. H.; Teitell, M. A.; Chiou, P. Y.; Zhang, D. D.; Wong, P. K. Detection of mRNA in Living Cells by Double-Stranded Locked Nucleic Acid Probes. *Analyst* **2013**, *138*, 4777–4785.
32. Riahi, R.; Long, M.; Yang, Y.; Dean, Z.; Zhang, D. D.; Slepian, M. J.; Wong, P. K. Single Cell Gene Expression Analysis in Injury-Induced Collective Cell Migration. *Integr. Biol.* **2013**, *6*, 192–202.
33. Link, S.; El-Sayed, M. A. Spectral Properties and Relaxation Dynamics of Surface Plasmon Electronic Oscillations in Gold and Silver Nanodots and Nanorods. *J. Phys. Chem. B* **1999**, *103*, 8410–8426.
34. Alkilany, A. M.; Nagaria, P. K.; Hexel, C. R.; Shaw, T. J.; Murphy, C. J.; Wyatt, M. D. Cellular Uptake and Cytotoxicity of Gold Nanorods: Molecular Origin of Cytotoxicity and Surface Effects. *Small* **2009**, *5*, 701–708.
35. Chithrani, B. D.; Ghazani, A. A.; Chan, W. C. W. Determining the Size and Shape Dependence of Gold Nanoparticle Uptake into Mammalian Cells. *Nano Lett.* **2006**, *6*, 662–668.
36. Rosi, N. L.; Mirkin, C. A. Nanostructures in Biodiagnostics. *Chem. Rev.* **2005**, *105*, 1547–1562.
37. Connor, E. E.; Mwamuka, J.; Gole, A.; Murphy, C. J.; Wyatt, M. D. Gold Nanoparticles are Taken up by Human Cells but Do Not Cause Acute Cytotoxicity. *Small* **2005**, *1*, 325–327.
38. Kamei, Y.; Suzuki, M.; Watanabe, K.; Fujimori, K.; Kawasaki, T.; Deguchi, T.; Yoneda, Y.; Todo, T.; Takagi, S.; Funatsu, T.; Yuba, S. Infrared Laser-Mediated Gene Induction in Targeted Single Cells *in Vivo*. *Nat. Methods* **2009**, *6*, 79–81.
39. Shamovsky, I.; Ivannikov, M.; Kandel, E. S.; Gershon, D.; Nudler, E. RNA-Mediated Response to Heat Shock in Mammalian Cells. *Nature* **2006**, *440*, 556–560.
40. Henjakovic, M.; Martin, C.; Hoymann, H. G.; Sewald, K.; Ressmeyer, A. R.; Dassow, C.; Pohlmann, G.; Krug, N.; Uhlig, S.; Braun, A. *Ex Vivo* Lung Function Measurements in Precision-Cut Lung Slices (PCLS) from Chemical Allergen-Sensitized Mice Represent a Suitable Alternative to *In Vivo* Studies. *Toxicol. Sci.* **2008**, *106*, 444–453.